*Research Article*

# Intuitionistic Fuzzy Hamacher Generalized Shapley Choquet Integral Operators Based Decision-Making Model for Feature Extraction and Automatic Material Classification in Mining Area Using Satellite Data

**Seema Khanum** [ID],[1] **M. Gunasekaran** [ID],[2] **S. V. Rajiga** [ID],[1] **A. Firos** [ID],[3] **and Kafui Tsoeke Agbevanu** [ID][4]

[1]*Department of Computer Science, Government Arts College, Salem 636007, India*
[2]*Department of Computer Science, Government Arts College, Dharmapuri 636705, India*
[3]*Department of Computer Science and Engineering, Rajiv Gandhi University, Doimukh 791112, India*
[4]*Department of Computer Science, Ho Technical University, P. O. Box HP 217, Ho, Ghana*

Correspondence should be addressed to A. Firos; firosabd@gmail.com and Kafui Tsoeke Agbevanu; kagbevanu@htu.edu.gh

The normal methods for monitoring environmental pollution with image data have many false positives. Therefore, this study is proposing a single-valued neutrosophic set (SVNS) (a variant of NS)-based method as a decision-making model using intuitionistic fuzzy Hamacher generalized Shapley Choquet integral operators for feature extraction and automatic material classification in mining area using satellite data. The experimental results show that this decision-making model using intuitionistic fuzzy Hamacher generalized Shapley Choquet integral operators for feature extraction and automatic material classification can better predict the presence of four heavy metals, i.e., vanadium(V), iron (Fe), copper (Cu), and nickel (Ni) in the study area than other methods. For vanadium metal, the determination accuracies, namely, producer accuracy, user accuracy, overall accuracy, and Kappa were 94.5%, 94.1%, 93.88%, and 0.93%, respectively. It was found that the estimated results and the distribution trend of heavy metals are almost the same as in actual ground measurements.

## 1. Introduction

The environmental pollution due to heavy metal mining is increasing day by day [1]. Geological Survey of India data say that India is consuming 4% of vanadium produced in the world, that is, about 85000 metric tons. In this arena, China is the largest player, who consumes 44% of this metal and they are producing 57% of globe's vanadium. The vanadium metal is noted for its toxicity [25]. The symptoms associated with vanadium poisoning are cough with sputum, wheezing, sore throat, headache, and rhinitis. The studies have shown that vanadate acts directly on the smooth muscle of the bronchi. It promotes the release of $Ca^{2+}$ in the cells by a mechanism involving the production of inositol triphosphate and inhibition of ATPase [6].

Vanadium has "insulin-like" action [7, 8], and this effect explains the observed hypoglycemia.

In remote sensing technology, we acquire information or data about the Earth's surface without actually being in contact with it [9]. The best example of remote sensing are our eyes. Human beings observe many things through the eyes without touching these things. However, our eyes are not sensitive to all parts of the electromagnetic spectrum. Our eyes are only sensitive to the visible part of the electromagnetic spectrum. Therefore, we as humans use a very small window of the electromagnetic spectrum. But there are some animals and birds which are more sensitive in other parts of the electromagnetic spectrum. For instance, the mammal bat has got a different kind of remote sensing technology. That means, it sends the echo pulses and records

the return pulses. Based on that, bat basically makes the assessment about its prey.

So, our eyes are only sensitive to the visible part and not the infrared or thermal infrared part of the electromagnetic spectrum. As a result, when we look at an object through a distance, we cannot assess the temperature of that object unless we know some other background information. Nowadays, various types of satellites are in space. These satellites are basically recording whatever the reflected or emitted energy reflected is. For reflected energy, we require some source. The best source available for us is the Sun. Sun during daytime illuminates the Earth, and whatever reflected energy reaching the satellite is recorded. All natural objects which are having temperature above absolute zero also emit energy. That energy can also be recorded in thermal part of the electromagnetic spectrum.

In remote sensing, reflected and emitted energies are recorded. Processing remote sensing data involves analysis of data and how to use this dataset. Various types of satellites generate huge amount of dataset. For instance, nowadays, people are using satellites for natural resource management, disaster management, civil engineering, and so on for various applications. In effect, there is an illumination source available to us from the Sun and the satellite. Moreso, different satellites may have ground stations and recording analysis facility on the ground. The reflected remote sensing requires the Sun as energy source, the radiation and the atmosphere in-between.

So, we are having a processing facility between the Earth and the Sun and whatever interactions the Sun has with different objects. For example, if the solar energy is falling on water, it will have a reflectance. If it is falling on the bare ground, it will have different reflectance. If it is on vegetation, it will have different reflectance. Therefore, the interaction with the target is important, and it is the basis for image making and image interpretation and analysis. We present the procedure we followed after the reflection going through the atmosphere and final recordings of the satellite. These satellites have different types of sensors. The different types of sensors were incorporated with the satellites to facilitate the transmission of data from satellite to ground stations of different satellites.

Additionally, data processing and analysis were performed. Data interpretation and analysis are much important because a lot of data nowadays is available but not much analysis or interpretations are being done. New innovations always require integration with other datasets while doing interpretation and analysis. The satellite reaches different types of objects on the Earth including buildings, roads, grasses, water bodies, and forests. The reflected energy, i.e., the reflected solar radiation goes back to the satellites through the atmosphere. During transmission, a lot of changes are introduced into the reflected radiation from the Earth towards the satellite. There is a need to correct the reflected transmission and enhance our image. This approach is employed in digital image processing, satellite data, and can be utilized in remote sensing.

Solar radiation which reaches the Earth has to go back to the satellite through the atmosphere again with component B. As energy travels from its source to a target, it will come in contact with and interact with that misfile. Initially, the energy from the source will interact with the target for a few seconds. When our solar radiation or reflected energy is going back from the Earth's surface towards the satellite, they may be obstructed by clouds. During the day, the passive remote sensing, the reflected part, and the clouds create problems. The major issue is that the satellite will record clouds but not the part of the Earth.

It must be noted that the atmosphere plays a very important role. While this solar radiation and the reflected solar radiation reach the satellite, then we have the C component which is the interaction with the target. Once the energy hits or the solar radiation hits the object or the target, it interacts with the target depending on the properties of both the target and the radiation. There are variations in properties resulting from different behaviors regarding whether the solar radiation is falling on a building or on a bare soil or on rock exposures or over the water body or vegetation. Therefore, the signatures that are reflected towards the satellite are also going to be different. This makes the basis of our image which can be depicted differently in digital values basically and assign these digital values different colors. This enable us to see things in different colors, and the D component is the recording of energy by the sensors. Once this reflected solar energy reaches the satellite, it is recorded by the sensors which are present. The recording systems are onboard of these different satellites.

After the energy has been scattered by the Earth, the reflected energy goes through direct misfile to the satellite. It has to pass through the atmosphere, and this can create some problems such as absorptions and scattering requiring a sensor in contact with the target to collect and record the electromagnetic radiation. Recording systems onboard of these satellites are also required. The satellites do not only record but also transmit the data towards the processing centre. Therefore, with appropriate setup for recording live data, as part of the Earth is being scanned by the satellite, the data are being recorded at the same time. Also, the data recorded are directly being broadcasted to Earth stations. The data about a particular part of the Earth are immediately received as the satellite passes over. The transmission, reception, and processing represent the E component. The transmission is done by the satellite and the energy is recorded by the onboard sensors. Often, the transmission is done in electronic/digital form. The transmissions received by Earth stations are broadcasted over different parts of the Earth in different countries. Initial data processing is done by the Earth stations after which advanced processing or digital image processing is carried out.

Component F involves the interpretation and analysis of the recorded image by onboard satellite sensors. The recorded image may initially not be the one transmitted from the object as expected or the differentiation between image and object. Therefore, a lot of processing is required. The first process is to correct the image and do radiometric corrections. There might be some problems with the sensor scanners that need to be corrected. Generally, these problems are corrected by the operators of the satellites or Earth

stations. During the analysis, decision is taken to remove the atmospheric distortions. Because the reflected energy is going through the atmosphere, this causes a lot of distortions in the data, ultimately in the images. The distortions need to be removed to make the image much sharper, more useful, and interpretable. Additionally, some advanced image processing techniques are applied. A few advanced image processing techniques exist of which pattern recognition or image classification is mainly used [3, 10].

USGS Landsat 8 Level 2, Collection 2, Tier 1 (LANSAT/LC08/C02/T1) dataset was collected by our team at a certain mining area to evaluate the method proposed and to prepare a forest density map. Using a satellite image, it is possible to prepare a land-use map or maybe a little logical map, that is, a structural map. All kinds of maps can then be derived using remote sensing data, which is explained under interpretation and analysis. Finally, the G component, that is, the application and the most important one is explained in Section 5. Satellite data analysis has a lot of applications. In some research studies, weather forecasting and weather monitoring were employed. Long-term data can be applied especially by climate change researchers in simple land map preparation, creation of land cover maps, forecast cover maps, vegetation density maps, and even agricultural production forecasting and mineral exploration [1, 11, 12].

Our environment may be polluted by pollutants from vehicles or industry doing coal burning or mining. Satellite images help recognize large areas of pollution created by fires, dust or sand storms, volcanic eruptions, large industrial sources, or the transport of man-made pollution from other regions. Smaller sources such as small industries or local roads will not be visible in satellite images. This study proposes a novel material detection technique specially tuned for vanadium metal detection to surpass this difficulty of detecting pollutants from small sources [13, 14]. Specifically, the study considered the metal vanadium as a focal point due to its toxicity at a time when more countries like India is coming to the arena of large-scale producers of vanadium metal through mining.

For image classification, the back propagation neural network (BPNN) is one of the most widely used neural network models. The BPNN model incorporates a hierarchical model for feature extraction and classification. In this study, we focus on defining a BPNN-based model for classifying the vanadium metal pollution within the satellite-collected images with the help of fuzzy clustering [15]. The traditional approach for image clustering based on neural networks has many false positives [13, 16, 17]. The stakeholders, for example, the environmentalists, find it difficult and tedious to make a decision to address the air pollution. Therefore, in this study, a novel fussy classification approach has been developed to address air pollution problems. Neutrosophic sets (NSs) are known for denoising, clustering, segmentation, and classification for various problems. Hence, the single-valued neutrosophic set (SVNS) (a variant of NS)-based method as a decision-making model using intuitionistic fuzzy Hamacher generalized Shapley Choquet integral operators for feature extraction and automatic material classification in mining area using satellite data is proposed here.

The rest of this study is structured as follows: Section 2 presents the background of neutrosophic sets based image classification techniques. The proposed method of the image classification and decision-making problem is proposed in Section 3. The experiment is presented in Section 4 in which we collected and preprocessed the USGS Landsat 8 Level 2, Collection 2, Tier 1 (LANDSAT/LC08/C02/T1) dataset at a certain mining area to evaluate our proposed method. Section 5 gives the experimental setup and some examples, and includes the conclusion and future work of this study.

## 2. The Background

Neutrosophic sets (NSs) are used for segmentation, denoising, and classification in many image processing applications. To avoid the uncertainty of efficient decision making in image processing techniques, NS has been incorporated [11, 18]. The NS domain constitutes three membership functions: true ($T$), indeterminacy ($I$), and false ($F$). For clustering, the image is transformed into NS domain. Different filters are used in this process. Median filter to calculate $T$ that iteratively calculates the best form of the image of $T$ and F function is one of the examples of such filter. Sobel, Prewitt, and the unsharp filter are used to calculate the indeterminacy neutrosophic subset I. The pixels whose I value is greater than a specific threshold are omitted from the categorization process in the clustering phase. Other pixels are categorized using the K-means [19].

The single-valued neutrosophic set (SVNS) is a form of NS which can be used in real world problems [20]. The SVNS is a generalization of classic set, fuzzy set, interval-valued fuzzy set, intuitionistic fuzzy set, and paraconsistent set [20, 21].

Flowchart extended FS data to NS (SNS, SVNS, and INS) is shown in Figure 1, where FS is the fuzzy set, NS is the neutrosophic set, SNS is the simplified neutrosophic set, SVNS is the single-valued neutrosophic set, INS is the interval neutrosophic set, IFS is the intuitionistic fuzzy set, and IVIFS is the interval-valued intuitionistic fuzzy set.

The SVNS: consider P to be a space of points (pixel), and let $p$ be a generic component in $P$ [22]. In SVNS, $S$ in $P$ is an object

$$S = \{\langle p, M_s(p), D_s(p), N_s(p)\rangle | p \in P\}, \tag{1}$$

where $M_S: P \longrightarrow [0, 1]$ is the truth-membership function, $D_S: P \longrightarrow [0, 1]$ is the indeterminacy-membership function, and $N_S: P \longrightarrow [0, 1]$ is the falsity-membership function. Thus, for each point $p$ in $P$, we have

$$0 \leq M_S(p) + D_S(p) + N_S(p) \leq 3. \tag{2}$$

As an extension of the SVNS, an INS is defined [20] by an object:

$$S = \{\langle p, \tilde{M}_S(p), \tilde{D}_S(p), \tilde{N}_S(p)\rangle | p \in P\}, \tag{3}$$

where $\tilde{M}_S$ is the truth-membership function, $\tilde{D}_S$ is the indeterminacy-membership function, and $\tilde{N}_S$ is the
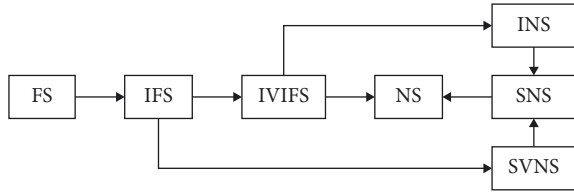
FIGURE 1: Flowchart extended FS data to NS (SNS, SVNS, and INS), IFS, and IVIFS.

falsity-membership function, such that for each point $p$ in $P$, we have

$$
\begin{aligned}
&\widetilde{M}_S(p) \subset [0,1], \\
&\widetilde{D}_S(p) \subset [0,1], \\
&\widetilde{N}_S(p) \subset [0,1]''.
\end{aligned}
\tag{4}
$$

An INS [23] can provide a value that varies for the "truth, indefiniteness, and falseness" rather than single values for each of these measures. For the INS, the interval neutrosophic number (INN) has been defined as "An object $\widetilde{x}$ given by the function $\widetilde{x} = \langle [M_{\widetilde{x}}^B, M_{\widetilde{x}}^A], [D_{\widetilde{x}}^B, D_{\widetilde{x}}^A], [N_{\widetilde{X}}^B, N_{\widetilde{X}}^A] \rangle$, where each module of $\widetilde{x}$ is an interval value."

### 2.1. The "Score, Accuracy, and Possibility Degree Functions" of INNs.

The score (S) and accuracy (A) functions of the INN, as proposed by Sahin [24], are defined.

"For an INN $\widetilde{y} = \langle [M_{\widetilde{y}}^B, M_{\widetilde{y}}^A], [D_{\widetilde{y}}^B, D_{\widetilde{y}}^A], [N_{\widetilde{y}}^B, N_{\widetilde{y}}^A] \rangle$, the score $S(\widetilde{y})$ and the accuracy $A(\widetilde{y})$ functions of $\widetilde{y}$ are, respectively, defined as follows:

$$
S(\widetilde{y}) = \frac{2 + \left( M_{\widetilde{y}}^B + M_{\widetilde{y}}^A \right) - 2\left( D_{\widetilde{y}}^B + D_{\widetilde{y}}^A \right) - \left( N_{\widetilde{y}}^B + N_{\widetilde{y}}^A \right)}{4},
\tag{5}
$$

where $\mathbf{S}(\widetilde{\mathbf{y}}) \in [-1,1]$.

$$
A(\widetilde{y}) = \frac{\left( M_{\widetilde{y}}^B + M_{\widetilde{y}}^A \right) - D_{\widetilde{y}}^B\left( 1 - M_{\widetilde{y}}^B \right) - D_{\widetilde{y}}^B\left( 1 - M_{\widetilde{y}}^B \right) - N_{\widetilde{y}}^A\left( 1 - D_{\widetilde{y}}^B \right) - N_{\widetilde{y}}^B\left( 1 - D_{\widetilde{y}}^A \right)}{2},
\tag{6}
$$

where $\mathbf{A}(\widetilde{\mathbf{y}}) \in [-1,1]$.

If $S(\widetilde{p}) > S(\widetilde{q})$, then "$\widetilde{p} \succ \widetilde{q}$," and if "$S(\widetilde{p}) = S(\widetilde{q})$" and "$A(\widetilde{p}) > A(\widetilde{q})$", then $\widetilde{p} \succ \widetilde{q}$, where $\widetilde{p}$ and $\widetilde{q}$ are the INNs. The possibility degree $B(\widetilde{p} \succ \widetilde{q})$ [25] of interval numbers $\widetilde{p} = [p^B, p^A]$ and $\widetilde{q} = [q^B, q^A]$ is given as

$$
B(\widetilde{p} \geq \widetilde{q}) = \max \left\{ 1 - \max \left\{ \frac{q^A - q^B}{p^A - p^B + q^A - q^B}, 0 \right\}, 0 \right\}.
\tag{7}
$$

### 2.2. Hamacher Operations.

As proposed by Hamacher [26], "Hamacher product" $\otimes_H$ and "Hamacher sum" $\oplus_H$ can be calculated as

$$
''M_z(x,y) = x \otimes_H y = \frac{xy}{z + (1-z)(x + y - xy)}, \quad z > 0'',
$$

$$
''S_z(x,y) = x \oplus_H y = \frac{x + y - xy - (1z\gamma)xy}{1 - (1-z)xy}, \quad z > 0'',
\tag{8}
$$

when $z = 1$, $\otimes_H$ and $\oplus_H$ reduces to "algebraic product and sum," respectively, as

$$
\begin{aligned}
&"M_1(x,y) = x, y" \\
&"S_1(\alpha, \beta) = \alpha + \beta - \alpha\beta",
\end{aligned}
\tag{9}
$$

and if $z = 2$, $\otimes_H$ and $\oplus_H$ reduce to the Einstein' "$t$-norm" and "$t$-conorm," respectively, as

$$
''M_2(x,y) = \frac{xy}{1 + (1-x)(1-y)}'', \quad S_2(x,y) = \frac{x+y}{1+xy}.
\tag{10}
$$

### 2.3. The Choquet Integral.

A $\lambda$-fuzzy measure $m: F(P) \longrightarrow [0,1]$, where $P = \{p_1, p_2, \ldots, p_n\}$ is a finite set of criteria that satisfies the following properties [27].

(i) $m(\varnothing) = 0, m(P) = 1$

(ii) if $A \subseteq B \subseteq X$, then $m(A) \leq m(B)$

(iii) $m(A \cup B) = m(A) + m(B) + \lambda m(A)m(B)$, $\lambda \in (-1, +\infty)$, $\forall A, B \in F(P)$ and $A \cap B = \varnothing$.

The condition (iii) reduces to the axiom of additive measure for $\lambda = 0$:

$$
m(A \cup B) = m(A) + m(B), \quad \forall A, B \subseteq P \text{ and } A \cap B = \varnothing.
\tag{11}
$$

If the elements in $P$ are independent, then

$$
m(A) = \sum_{p_c \in A} m(\{p_c\}).
\tag{12}
$$

This can be normalized as proposed by Sugeno [27] as

$$
"n(P) = \begin{cases} \dfrac{1}{\lambda}\left( \prod_{c=1}^{max} [1 + \lambda n(P_c)] - 1 \right), & \text{if } \lambda \neq 0, \\[4mm] \sum_{c=1}^{max} n(P_c), & \text{if } \lambda = 0. \end{cases}
\tag{13}
$$

If $S \subseteq P$, then

$$
"n(S) = \begin{cases} \dfrac{1}{\lambda}\left( \prod_{p_c \in S} [1 + \lambda n(p_c)] - 1 \right), & \text{if } \lambda \neq 0, \\[4mm] \sum_{c=1}^{max} n(p_c), & \text{if } \lambda = 0. \end{cases}
\tag{14}
$$

$\lambda$ can be determined with equation (13) and $n(P) = 1$:

$$\lambda + 1 = \prod_{c=1}^{\max}\left(1 + \lambda n(p_c)\right). \qquad (15)$$

The Choquet integral [28] based on the fuzzy measure is given as follows.

"If $g$ is a positive real-valued function on $P = \{p_1, p_2, \ldots, p_{\max}\}$ and $n$ is a fuzzy measure on $P$, the discrete Choquet integral of $g$ with respect to $n$, denoted by $\chi_n(g)$, is

$$P_n(g) = \sum_{c=1}^{\max} g\left(p_{(c)}\right) \cdot \left(n\left(B_{(c)}\right) - n(B_{i-1})\right), \qquad (16)$$

where $(\cdot)$ indicates a permutation on $P$, such that $g(p_{(1)}) \geq g(p_{(2)}) \geq \cdots \geq g(p_{(\max)})$, with $B_{(i)} = \left\{p_{(1)}, p_{(2)}, \ldots, p_{(i)}\right\}$ for $c \geq 1$ and $B_{(0)} = \varnothing$."

The "interval neutrosophic numbers Choquet integral (INNCI)" operator [29] for an INN function $g: P \longrightarrow B$ on $P$ with respect to a fuzzy measure $n$ on $P$ is given by

$$\int \mathrm{gdn} = \sum_{c=1}^{\max} g\left(P_{(c)}\right)\left(n\left(P_{(c)}\right) - n\left(P_{(c-1)}\right)\right). \qquad (17)$$

If $n$ is a fuzzy measure on a finite set $P$ and $\tilde{y}_d = \left\{[M_{y_d}^B, M_{y_d}^A], [D_{y_d}^B, D_{y_d}^A], [N_{y_d}^B, N_{y_d}^A]\right\}$ $(d = 1, 2, \ldots, n)$ are INNs on $P$, then the INHPCI can be defined as follows [30]:

$$\mathrm{INHPCI}\left(\tilde{y}_1, \tilde{y}_2, \ldots, \tilde{y}_d\right) = \frac{\oplus_{H\,d=1}^{n}\left(n\left(B_{(d)}\right) - n\left(B_{(d-1)}\right)\right)\left(1 + V\left(\tilde{y}_{d-1}\right)\right)\tilde{y}_d}{\sum_{d=1}^{n}\left(n\left(B_{(d)}\right) - n\left(B_{(d-1)}\right)\right)\left(1 + V\left(\tilde{y}_d\right)\right)}, \qquad (18)$$

where $(\cdot)$ indicates a permutation on $\{1, 2, 3, \ldots, n\}$ with $\tilde{y}_{(1)} \succ \tilde{y}_{(2)} \succ \cdots \succ \tilde{y}_{(n)}$ and $B_{(d)} = \{(1), \ldots, (d)\}$, with the convention $B_{(0)} = \varnothing$, $V(\tilde{y}_{(c)}) = \sum_{d=1}^{n}\left(n(B_{(d)}) - n(B_{(d-1)})\right)$, $\epsilon$, $(\tilde{y}_{(i)}, \tilde{y}_{(j)})$, $d \neq i$
where $\epsilon$, $(\tilde{y}_{(i)}, \tilde{y}_{(j)})$ denotes the support of $\tilde{y}_{(i)}$ from $\tilde{y}_{(j)}$ and have the following mentioned properties.

(i) $(\tilde{y}_{(i)}, \tilde{y}_{(j)})$, $\epsilon \in [0, 1]$
(ii) $\epsilon$, $(\tilde{y}_{(i)}, \tilde{y}_{(j)}) = \epsilon$, $(\tilde{y}_{(i)}, \tilde{y}_{(j)})$

(iii) $\epsilon$, $(\tilde{y}_{(i)}, \tilde{y}_{(j)})$, $\geq \epsilon$, $(\tilde{y}_{(i)}, \tilde{y}_{(j)})$ if $d(\tilde{y}_{(i)}, \tilde{y}_{(j)})$ $< d(\tilde{y}_{(s)}, \tilde{y}_{(t)})$

where $d$ denotes the Hamming distance of INNs.

Also, if $\tilde{y}_j = \left\{[M_{y_j}^B, M_{y_j}^A], [D_{y_j}^B, D_{y_j}^A], [N_{\beta_j}^B, N_{\beta_j}^A]\right\}$ $(d = 1, 2, \ldots, n)$ are INNs on a finite set $P$, then for a fuzzy measure $n$ on $P$, the INHPCI can be expressed as [30]

$$INHPCI\left(\tilde{y}_1, \tilde{y}_2, \ldots \tilde{y}_n\right)$$

$$= \Bigg\{ \Bigg[ g^{-1}\left(\frac{\sum_{d=1}^{\max}\left(\left(n\left(B_{(d)}\right) - n\left(B_{(d-1)}\right)\right)\left(1 + V\left(\tilde{x}_{(d)}\right)\right)\right)g\left(M_{x_j}^B\right)}{\sum_{d=1}^{n}\sum_{d=1}^{n}\left(\left(n\left(B_{(d)}\right) - n\left(B_{(d-1)}\right)1 + V\left(\tilde{x}_{(d)}\right)\right)\right)}\right), g^{-1}\left(\frac{\sum_{d=1}^{\max}\left(\left(n\left(B_{(d)}\right) - n\left(B_{(d-1)}\right)\right)\left(1 + V\left(\tilde{x}_{(d)}\right)\right)\right)g\left(M_{x_j}^A\right)}{\sum_{d=1}^{\max}\sum_{d=1}^{\max}\left(\left(n\left(B_{(d)}\right) - n\left(B_{(d-1)}\right)1 + V\left(\tilde{x}_{(d)}\right)\right)\right)}\right) \Bigg],$$

$$\Bigg[ f^{-1}\left(\frac{\sum_{d=1}^{\max}\left(\left(n\left(B_{(d)}\right) - n\left(B_{(d-1)}\right)\right)\left(1 + V\left(\tilde{x}_{(d)}\right)\right)\right)f\left(D_{x_j}^B\right)}{\sum_{d=1}^{\max}\left(\left(n\left(B_{(d)}\right) - n\left(B_{(d-1)}\right)\right)\left(1 + V\left(\tilde{x}_{(d)}\right)\right)\right)}\right), f^{-1}\left(\frac{\sum_{d=1}^{\max}\left(\left(n\left(B_{(d)}\right) - n\left(B_{(d-1)}\right)\right)\left(1 + V\left(\tilde{x}_{(d)}\right)\right)\right)f\left(D_{x_j}^B\right)}{\sum_{d=1}^{\max}\left(\left(n\left(B_{(d)}\right) - n\left(B_{(d-1)}\right)\right)\left(1 + V\left(\tilde{x}_{(d)}\right)\right)\right)}\right) \Bigg],$$

$$\Bigg[ f^{-1}\left(\frac{\sum_{d=1}^{\max}\left(\left(n\left(B_{(d)}\right) - n\left(B_{(d-1)}\right)\right)\left(1 + V\left(\tilde{x}_{(d)}\right)\right)\right)f\left(N_{x_j}^B\right)}{\sum_{d=1}^{\max}\left(\left(n\left(B_{(d)}\right) - n\left(B_{(d-1)}\right)\right)\left(1 + V\left(\tilde{x}_{(d)}\right)\right)\right)}\right), f^{-1}\left(\frac{\sum_{d=1}^{\max}\left(\left(n\left(B_{(d)}\right) - n\left(B_{(d-1)}\right)\right)\left(1 + V\left(\tilde{x}_{(d)}\right)\right)\right)f\left(N_{x_j}^A\right)}{\sum_{d=1}^{\max}\left(\left(n\left(B_{(j)}\right) - n\left(B_{(d-1)}\right)\right)\left(1 + V\left(\tilde{x}_{(d)}\right)\right)\right)}\right) \Bigg] \Bigg\}. \qquad (19)$$

Equation (19) expresses the INPCI operator in terms of the additive generators [31], $f$ and $g$ of "Hamacher $t$-norm and $t$-conorm."

Also, if $\tilde{x}_d = \{[M_{x_d}^B, M_{x_d}^A], [D_{x_d}^B, D_{x_d}^A], [N_{x_d}^B, N_{x_d}^A]\}$ $(d = 1, 2, \ldots, n)$ are INNs on a finite set $X$, then for a fuzzy measure $m$ on $X$, the "interval neutrosophic Hamacher

power geometric Choquet integral operator (INHPGCI)" is given as follows:

$$\text{INHPGCI}\left(\widetilde{x}_1, \widetilde{x}_2, \ldots, \widetilde{x}_n\right) = \overset{\max}{\underset{H}{\otimes}}\,\widetilde{x}_{(n)}^{\left(n\left(B_{(d)}\right)-n\left(B_{(d-1)}\right)\right)\left(1+V\left(\widetilde{x}_{(d)}\right)\right)/\sum_{d=1}^{\max}\left(n\left(B_{(d)}\right)-n\left(B_{(d-1)}\right)\right)\left(1+V\left(\widetilde{x}_{(d)}\right)\right)}. \tag{20}$$

## 3. Proposed Model

The proposed decision-making model using intuitionistic fuzzy Hamacher generalized Shapley Choquet integral operators for feature extraction and automatic material classification with mining area satellite data employs the back propagation neural network (BPNN) algorithm [32]. There is an express training stage with known vanadium pixel set MFCC corpus. Training MFCC corpus is based on vanadium image properties given in illustrative example of Section 4. Input image signals are taken from noisy image corpus LANDSAT/LC08/C02/T1. Using the spectral subtraction method, the noise is removed from the input. Speech signal is divided into small frames of N samples; with this, the adjacent frames are overlapped by N-M samples. This experiment puts standard value for $N = 256$ and $M = 100$. Hamming windows are created with the frames to avoid any cutoffs at the ends. From this, hamming windows future vectors are extracted with the MFCC algorithm. After the clusters are created by the intuitionistic fuzzy Hamacher generalized Shapley Choquet integral operators fuzzy c-mean (HGSCIO-FCM) clustering method, they are arranged in proper format to feed into the artificial neural Network for recognition. In the training stage, the weights of the feed forward neural network were given by some arbitrary values that were based on vanadium image properties given in illustrative example of Section 4 and is then tuned for the optimal value during the iterative learning procedure with the help of the BPNN algorithm. In the testing stage, the neural network is tested against a variety of test samples of image (MFFC feature vector sets) to ensure whether the acquired system correctly categorizes the image fragment into vanadium and other metal clusters. Now, authenticity of metal detection is suggested as end result using vanadium/other metal image corpus. The process is given, as shown in Figure 2 and Algorithm 1.

### 3.1. Feature Extraction. Readers can refer to the steps for calculating MFCC in [10].

### 3.2. The Material Classification Process with HGSCIO-FCM.
The proposed algorithm classifies the pixels according to fuzzy rules that is automatically generated from the sample data with respect to edge strength values of pixels. A two-step learning of the neurofuzzy network is done on a training set for making the fuzzy rule base for pixel classification.

Here, each datum is a vector of the following form: $(E(1)_{ij}, \ldots, E®_{ij}, c1, c2, c3)$, where c1, c2, and c3 represent the binary values which designate the association of a pixel to the classes C1, C2, and C3. In the first learning step, parameters of fuzzy rules are obtained through an unsupervised learning algorithm based on a competitive scheme. In the second learning step, fuzzy rule parameters are further optimized via a supervised learning algorithm based on a gradient descent technique [2]. Once learning is completed, the neurofuzzy network encodes a set of fuzzy classification rules in its topology, which is explained in HGSCIO-FCM Decision-Making Model for Material Detection. This can be used to perform classification of pixels in any image.

### 3.3. HGSCIO-FCM Decision-Making Model for Material Detection. This section proposes a novel multicriteria decision-making model for material image clustering with INHPCI and INHPGCI operators.

Assume that calculation data of the alternatives are provided by INNs and there is an interrelationship among the attributes. "$P = \{p_1, p_2, \ldots, p_m\}$" be a set of pixels from various related metal image sets grabbed through satellite and let "$X = \{X_1, X_2, \ldots, X_n\}$" be a collection of probable pixels sets for classifying a portion of image as vanadium. The categorization statement of each image set "$p_c (c = 1, 2, \ldots, m)$" corresponding to probable pixels sets "$X_j (d = 1, 2, \ldots, n)$" is stated by the INN "decision matrix $\widetilde{W} = (\widetilde{y}_{cd})_{m \times n}$" where each "$\widetilde{y}_{cd} (c = 1, 2, \ldots, m; d = 1, 2, \ldots, n)$" is an INN and is specified by

$$\widetilde{y}_{cd} = \left[M_{\widetilde{y}_{cd}}^B, M_{\widetilde{y}_{cd}}^A\right], \left[D_{\widetilde{y}_{cd}}^B, D_{\widetilde{y}_{cd}}^A\right], \left[N_{\widetilde{y}_{cd}}^B, N_{\widetilde{y}_{cd}}^A\right], \quad (c = 1, 2, \ldots, m; d = 1, 2, \ldots, n). \tag{21}$$

The selection procedure of image fragment with highest probable pixels qualified as vanadium includes the following steps (clustering in Step 6 of Algorithm 1).

*Step 1.* Calculate the score $S(\widetilde{y}_{cd})$ of every INN with equation (5) to rearrange "$\widetilde{y}_{cd} (c = 1, 2, \ldots, m)$" as

$$\widetilde{y}_{c(1)} \succ \widetilde{y}_{c(2)} \succ \cdots \succ \widetilde{y}_{c(n)}. \tag{22}$$
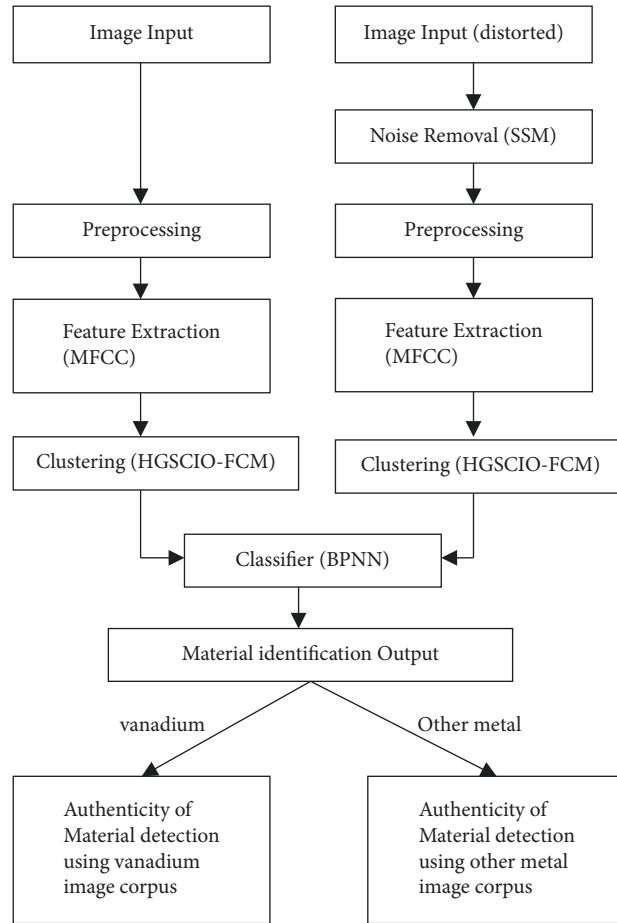
FIGURE 2: Block diagram of the proposed robust and fast system to cluster the material samples.

---

Input: image signals of LANDSAT/LC08/C02/T1 dataset.
Output: authenticity of material detection/classification.
Start
(1) Input noisy image signals
(2) Noise is removed using the spectral subtraction method
(3) image signal is divided into frames
(4) Frames are windowed with Hamming window
(5) Feature vectors are extracted from the speech signal using the MFCC algorithm.
(6) Clusters are created by the intuitionistic fuzzy Hamacher generalized Shapley Choquet integral operators fuzzy c-mean (HGSCIO-FCM) clustering method, arranged in proper format to feed into the artificial neural network for **classification**.
(7) Training stage: weights of the feed forward neural network were given by some arbitrary values and then tuned for optimal during the iterative learning procedure with the help of the back propagation algorithm.
(8) Testing stage: the neural network is tested against a variety of test samples of image to ensure whether the acquired system correctly categorizes the metal into vanadium and other metal parts.
(9) Authenticity of image classification is done **using vanadium/other metal image corpus**.
Stop

ALGORITHM 1: Authenticity of material detection/classification using vanadium/other metal image corpus.

*Step 2.* Calculate the supports,

$$\varepsilon\left(\widetilde{y}_{cd}, \widetilde{y}_{ce}\right) = 1 - I\left(\widetilde{y}_{cd}, \widetilde{y}_{ce}\right), \quad (c = 1, 2, \ldots, m; d, e = 1, 2, \ldots, n; d \neq e). \tag{23}$$

Here, "normalized Hamming distance" between any two INNs is $I(\tilde{y}_{cd}, \tilde{y}_{ce})$.

**Step 3.** Now, we calculate the weights of INNs "$\tilde{y}_{cd}$ ($c = 1, 2, \ldots, n$)" with

$$\omega_{cd} = \frac{\left(\left(n(B_{(d)}) - n(B_{(d-1)})\right)\left(1 + \mathcal{O}(\tilde{y}_{(cd)})\right)\right)}{\sum_{d=1}^{\max}\left(\left(n(B_{(d)}) - n(B_{(d-1)})\right)\left(1 + \mathcal{O}(\tilde{y}_{(cd)})\right)\right)}, \quad (24)$$

where

$$\mathcal{O}(\tilde{y}_{(cd)}) = \sum_{\substack{e=1 \\ e \neq d}}^{\max} \left(n(B_{(d)}) - n(B_{(d-1)})\right) \in (\tilde{y}_{(cd)}, \tilde{y}_{(ce)}), \quad (e = 1, 2, \ldots, n), \quad (25)$$

$\omega_{cd} > 0$, and $\sum \omega_{cd} = 1_{\max=1}$ ($C = 1, 2, \ldots, m$).

**Step 4.** Identify the fuzzy degree for all of the material factors $X_d$ ($d = 1, 2, \ldots, n$), and with equation (14), the fuzzy degree $n(S)$ of all $S \subseteq P$ can be calculated, where $\lambda$ can be calculated with equation (15).

**Step 5.** Identify $\tilde{y}_c$ of each alternative $p_c$ ($c = 1, 2, \ldots, m$) with equation (18) of INHPCI or equation (20) of INHPGCI.

**Step 6.** Identify the score and accuracy "$S(\tilde{x}_c)$, $S(\tilde{y}_c)$ ($c = 1, 2, \ldots, m$)" of the aggregated assessment "$\tilde{y}_c$ ($c = 1, 2, \ldots, m$)" consistent to all attributes "$p_c$ ($c = 1, 2, \ldots, m$)" and take the utmost accurate pixel set

**Step 7.** End.

## 4. Experimental Results

In the study, the image vectors are categorized into vanadium/other metals with the help of the pixel classification algorithm devised in MATLAB. From the classified image sample, the highest probable clusters of intended material are extracted. Afterwards, automated groping is done with intuitionistic fuzzy Hamacher generalized Shapley Choquet integral operators fuzzy c-mean (HGSCIO-FCM) to divide vanadium and other metal pixel values. An automated pixel set categorization is productively done by HGSCIO-FCM. Here, HGSCIO-FCM has to be trained prior to the real classification. The HGSCIO-FCM is used to obtain efficient and speedy performance of an architecture. The study claims that for vanadium and other metal pixel recognition, the system is 92% and 100% efficient, respectively. The average performance of the system is reported as 96.55%.

*4.1. Data Source.* The study uses the USGS Landsat 8 Level 2, Collection 2, Tier 1 (LANDSAT/LC08/C02/T1) dataset provided by USGS (United States Geological Survey). This dataset was collected by USGS with Landsat 8 OLI/TIRS sensors. It contains atmospherically corrected surface reflectance and land surface temperature data. This dataset is a culmination of orthorectified surface reflectance derived from (5 visible-near-infrared (VNIR) bands, 2 short-wave infrared (SWIR) bands) set, an orthorectified surface

temperature derived from thermal infrared (TIR) band, intermediate bands used in calculation of the ST products, and QA bands. The collected data contain the standardized reference grid of overlapping images with 170 km × 183 km.

Landsat satellites image the entire Earth's surface at a 30-meter resolution about once every two weeks including multispectral and thermal data. Landsat data are processed and hosted at the USGS's Earth Resources Observation and Science (EROS) Centre in Sioux Falls, South Dakota. The USGS Landsat 8 Level 2, Collection 2, Tier 1 (LANDSAT/LC08/C02/T1) [33] data in Earth Engine in its raw form, as surface reflectance, TOA-corrected reflectance, and in various ready-to-use computed products, such as NDVI and EVI vegetation indices, are available for download at no charge from Earth Explorer [34].

The dataset LANDSAT/LC08/C02/T1 used for this research contains a set of organised images, which is collected through Landsat satellite that orbits the Earth at 900 km (559 mi) in a Sun-synchronous, near-polar orbit (99.2 degrees inclination), circled the Earth every 103 minutes, and 18-day repeat cycle with an equatorial crossing time of 9 : 45 a.m. ±15 minutes.

Landsat 2 carried the sensors, the return beam vidicon (RBV) and the multispectral scanner system (MSS). The RBV sensor utilized vidicon tube instruments containing an electron gun that read images from a photoconductive faceplate. The data stream received from the satellite was analog-to-digital preprocessed to correct for radiometric and geometric errors. It has 3-axis stabilized using 4 wheels to ±0.7° attitude control and twin solar array paddles (single-axis articulation). For data reception, transmission uses S-band and very high frequency (VHF) communications and hydrazine propulsion system with 3 thrusters.

The Tier 1 data obtained contain the data that meet geometric and radiometric quality requirements. The Landsat 8 also collects Tier 2 and Tier 3 data. Tier 2 has data that do not meet the Tier 1 requirements. Tier 3 has real-time (RT) data that have not yet been evaluated, that is, the data collected in real-time. Examples for Landsat 8 datasets are given in Table 1.

As mentioned earlier, Landsat 2 has the return beam vidicon (RBV) sensor that has 80-meter ground resolution and has three cameras operating in band 1 visible blue-green (475–575 nm), band 2 visible orange-red (580–680 nm), and band 3 visible red to near-infrared (690–830 nm).

TABLE 1: Examples for Landsat 8 datasets.

| ID | Description |
|---|---|
| LANDSAT/LC08/C01/T1_RT | Landsat 8, Collection 1, Tier 1 + real-time |
| LANDSAT/LC08/C01/T1 | Landsat 8, Collection 1, Tier 1 only |
| LANDSAT/LC08/C01/T2 | Landsat 8, Collection 1, Tier 2 only |

Additionally, the MSS sensors were line-scanning devices observing the Earth perpendicular to the orbital track. MMS also covers the 80-meter ground resolution with band 4 visible green (0.5-0.6 $\mu$m), band 5 visible red (0.6-0.7 $\mu$m), band 6 near-infrared (0.7-0.8 $\mu$m), and band 7 near-infrared (0.8–1.1 $\mu$m) cameras. So, the proposed mechanism is able to tackle the transmission ranges, since these cameras are working in all visible spectrum of light.

The datasets given in the example above contain raw data, T1 or T2 images, TOA (top-of-atmosphere reflectance), SR (surface reflectance), and LST (land surface temperature). An example of image available in LANDSAT/LC08/C02/T1 is shown in Figure 3.

*4.2. Illustrative Example.* Here, an illustrative example is presented as a demonstration of the projected MCDM model for pixel set clustering with an intention to detect vanadium metal pollution under the "interval neutrosophic environment."

Vanadium is a silvery-white, ductile, metallic-looking solid. Assume that an observatory is performing metal classification on four sets of pixels "$P = \{p_1, p_2, p_3, p_4\}$" based on the following factors to detect the picture area with the highest vanadium pollution/detection.

(1) $X1$: silvery-white

(2) $X2$: ductile

(3) $X3$: metallic-looking



FIGURE 3: Example image available in LANDSAT/LC08/C02/T1.

(4) $X4$: solid

Assume that we have the four pixel sets "$p_c$ ($c = 1, 2, 3, 4$)," which need to be classified on metal properties "$X_d$ ($d = 1, 2, 3, 4$)" and are expressed as interval neutrosophic decision matrix "$\widetilde{W} = (\widetilde{x}_{cd})_{4 \times 4}$" as given in Table 2, where each "$\widetilde{x}_{cd}$ ($c = 1, 2, 3, 4$; $d = 1, 2, 3, 4$)" is an INN and signifies the detection property of the $c^{\text{th}}$ pixel set "$p_c$ ($c = 1, 2, 3, 4$)" under the $d^{\text{th}}$ factor "$X_d$ ($d = 1, 2, 3, 4$)." The calculation of the $c^{\text{th}}$ pixel set "$p_c$ ($c = 1, 2, 3, 4$)" under the $d^{\text{th}}$ factor "$X_d$ ($d = 1, 2, 3, 4$)" has been accomplished according to the classification report. The "interval neutrosophic decision matrix" is created as given in Table 2.

*Step 8.* Recognizing the fuzzy quantity $n(X_d)$ for each factor "$X_d$ ($d = 1, 2, \ldots, n$)" that quantifies the degree of relevance of each factor $n_d$ ($d = 1, 2, \ldots, n$). The following "fuzzy measure" of each factor is assumed as per the expert estimation:

$$n(\{X_1\}) = 0.26, n(\{X_2\}) = 0.21, n(\{X_3\}) = 0.17 \text{ and } n(\{X_4\}) = 0.23. \tag{26}$$

From (15), we get $\lambda = 0.43$, and using (14), we have

$$
\begin{aligned}
n(\{X_1, X_2\}) &= 0.4845, & n(\{X_1, X_3\}) &= 0.4581, & n(\{X_1, X_4\}) &= 0.5157, \\
n(\{X_2, X_3\}) &= 0.3899, & n(\{X_2, X_4\}) &= 0.4828, & m(\{X_3, X_4\}) &= 0.4279 \\
n(\{X_1, X_2, X_3\}) &= 0.7110, & n(\{X_1, X_2, X_4\}) &= 0.7834, & n(\{X_1, X_3, X_4\}) &= 0.7345 \\
n(\{X_2, X_3, X_4\}) &= 0.6755, & n(\{X_1, X_2, X_3, X_4\}) &= 1.
\end{aligned}
\tag{27}
$$

*Step 9.* The score values "$S(\widetilde{x}_{cd})$ ($c = 1, 2, 3, 4$; $d = 1, 2, 3, 4$)" of every "$\widetilde{x}_{cd}$ ($c = 1, 2, 3, 4$; $d = 1, 2, 3, 4$)" are estimated with equation (5) and given in Table 3.

The score values of "$\widetilde{x}_{1(d)}$ ($d = 1, 2, 3, 4$)" of the 1$^{\text{st}}$ pixel set $p_1$ are $S(\widetilde{x}_{1(1)}) = 0.0999, S(\widetilde{x}_{1(2)}) = 0.1349, S(\widetilde{x}_{1(3)}) = 0.0301$, and $S(\widetilde{x}_{1(4)}) = 0.1499$. Since $S(\widetilde{x}_{1(4)})$

$> S(\widetilde{x}_{1(2)}) > S(\widetilde{x}_{1(1)}) > S(\widetilde{x}_{1(3)})$ for the 1$^{\text{st}}$ pixel set, $p_1$, the partial evaluations $\widetilde{x}_{1(d)}$, where $d = 1, 2, 3, 4$, are rearranged as $\widetilde{x}_{1(4)} \succ \widetilde{x}_{1(2)} \succ \widetilde{x}_{1(1)} \succ \widetilde{x}_{1(3)}$ (Figure 4).

Then, the "fuzzy measure" for each of metal appearance factors "$X_d$ ($d = 1, 2, 3, 4$)" for th$^{\text{e}}$ 1st pixel set $p_1$ is given as

TABLE 2: The INN decision matrix $\widetilde{\mathbf{W}} = (\widetilde{\mathbf{x}}_{\mathbf{cd}})_{4 \times 4}$.

|  | $P_1$ | $P_2$ | $P_3$ | $P_4$ |
|---|---|---|---|---|
| $P_1$ | $\langle [0.5, 0.6], [0.4, 0.5], [0.6, 0.7] \rangle$ | $\langle [0.5, 0.6], [0.4, 0.6], [0.5, 0.6] \rangle$ | $\langle [0.4, 0.6], [0.4, 0.5], [0.7, 0.8] \rangle$ | $\langle [0.4, 0.5], [0.3, 0.4], [0.6, 0.7] \rangle$ |
| $P_2$ | $\langle [0.7, 0.8], [0.3, 0.4], [0.3, 0.7] \rangle$ | $\langle [0.7, 0.9], [0.2, 0.5], [0.2, 0.4] \rangle$ | $\langle [0.4, 0.5], [0.1, 0.2], [0.3, 0.4] \rangle$ | $\langle [0.3, 0.4], [0.2, 0.3], [0.4, 0.5] \rangle$ |
| $P_3$ | $\langle [0.5, 0.6], [0.2, 0.3], [0.4, 0.6] \rangle$ | $\langle [0.6, 0.7], [0.3, 0.4], [0.4, 0.5] \rangle$ | $\langle [0.5, 0.8], [0.4, 0.5], [0.3, 0.4] \rangle$ | $\langle [0.6, 0.9], [0.4, 0.5], [0.2, 0.4] \rangle$ |
| $P_4$ | $\langle [0.8, 0.9], [0.1, 0.3], [0.2, 0.4] \rangle$ | $\langle [0.6, 0.8], [0.2, 0.4], [0.3, 0.5] \rangle$ | $\langle [0.6, 0.7], [0.5, 0.7], [0.6, 0.8] \rangle$ | $\langle [0.5, 0.8], [0.5, 0.6], [0.2, 0.4] \rangle$ |

$$n(S_{1(1)}) = n(\{X_{(4)}\}) = 0.31 \, ; \, m(A_{1(2)}) = n(\{X_{(4)}, X_{(2)}\}) = 0.4719,$$
$$n(S_{1(3)}) = n(\{X_{(4)}, X_{(2)}, X_{(1)}\}) = 0.8824, n(S_{1(4)}) = n(\{X_{(4)}, X_{(2)}, X_{(1)}, X_{(3)}\}) = 1. \tag{28}$$

As a result, the ranking order of the "partial" estimations $\widetilde{x}_{cd} (c = 2, 3, 4; d = 1, 2, 3, 4)$ and "fuzzy measures" of the material $S_c (c = 2, 3, 4)$ based on the factors $X_d (d = 1, 2, 3, 4)$ is given in Table 4.

*Step 10.* Associated weights "$\omega_{cd} (c = 1, 2, \dots m; d = 1, 2, \dots. n) =$" are calculated with equations (23) and (24). The calculated weights are given in "Table 5."

*Step 11.* For various values of $z$, applying equation (19) of the INHPCI operator, the total evaluation outcome $\widetilde{x}_c (c = 1, 2, 3, 4)$ of each pixel set "$p_c (c = 1, 2, 3, 4)$" is computed as given in Table 6 and its variations are shown in Figure 5.

*Step 12.* From Table 6, we can conclude that even if the total calculations of "$\widetilde{x}_c (c = 1, 2, 3, 4)$" conforming to each pixel set $p_c (c = 1, 2, 3, 4)$ is dissimilar, the best ranking value is $\widetilde{x}_2$. So, $p_2$ is the highly preferable pixel set for classifying it as vanadium.

The screenshot of the HGSCIO-FCM based satellite image segmentation and classification application is shown in Figure 6.

The classification accuracy of the 4 features of 4 metals (vanadium, iron, copper, and nickel), namely, $X_1, X_2, X_3$, and $X_4$ was taken. The properties of these metals are given in Table 7.

The charts in Figure 7 show the classification accuracy of the four features using trained BPNN models that is using HGSCIO-FCM at four user levels. From this comparative study, it is inferred that no matter which user side the BPNN model is used, the HGSCIO-FCM classification-based BPNN system outperforms the other classification models. On the other hand, it is indicated that the HGSCIO-FCM-based classification is more robust.

Experiments with laboratory data: in order to verify the performance of BPNN models that is using HGSCIO-FCM system for material classification, experiments are realized on the laboratory data. The classification process of an image in different stages of the implemented BPNN model that is using HGSCIO-FCM is shown in Figure 8. The final detection cluster of vanadium through the implemented model is shown in Figure 9.

For vanadium metal, the determination accuracies, namely, producer accuracy, user accuracy, and overall accuracy were 94.50%, 94.10%, and 93.88%, respectively. It was found that the estimated results and the distribution trend of heavy metals are almost the same as in actual ground measurements. Standard interpretation values for image processing, PSNR (peak-to-signal noise ratio), and Kappa coefficient (accuracy assessment parameters) of the processed system were 55.7 dB and 0.93, respectively. That gives a good accuracy of the clustering system with the proposed model. Average elapsed time of the implemented BPNN image clustering model that is using HGSCIO-FCM is 4.0134 seconds.

As a comparative study, the proposed method was also tested with Landsat 3 and Landsat 4 datasets [34]. Readers must note that the Landsat 4 dataset is generated through satellites with reception ranges asymmetric. The investigation found that with Landsat 3 dataset, the determination accuracies, namely, producer accuracy, user accuracy, and overall accuracy were 93.99%, 93.88%, and 93.94%, respectively. The similar results were achieved with the Landsat 4 dataset too. This shows that the accuracy of the proposed method is not changing with the change in datasets of similar nature.

The proposed method is also tested with the Landsat 9 real-time dataset provided through [34]. Landsat 9 is processed into the Landsat Collection 2 inventory structure in the Worldwide Reference System-2 (WRS-2) path/row system, with swath overlap (or sidelap) varying from 7% at the equator to a maximum of approximately 85% at extreme latitudes. All Landsat 9 data products are available for download through the USGS Earth Resources Observation and Science (EROS) Centre at no charge. Since Landsat 9 is imaging global landmasses and nearshore coastal regions, including islands at solar elevation angles greater than 5 degrees that were not always routinely collected prior to Landsat 8, the determination accuracies, namely, producer accuracy was comparatively high and that was 96.81%. On the other side, the user accuracy was found to be compromised, which was 89.11%. The reduced accuracy may be due to receiving reception speed fluctuation of the realtime data which will be rectified in the future.

Landsat Thematic Mapper (TM)/Enhanced Thematic Mapper (ETM+) dataset is available at [35] to detect and map deforestation and forest degradation. TM data are sensed in seven spectral bands simultaneously. Band 6 senses thermal (heat) infrared radiation. The intuitionistic fuzzy Hamacher generalized Shapley Choquet

Table 3: The score values of $\widetilde{x}_{c\,d}$ equivalent to the decision matrix $\widetilde{W}$.

|        | $X_1$  | $X_2$  | $X_3$  | $X_4$  |
|--------|--------|--------|--------|--------|
| $p_1$  | 0.0999 | 0.1349 | 0.0301 | 0.1499 |
| $p_2$  | 0.2861 | 0.1840 | 0.2999 | 0.3999 |
| $p_3$  | 0.1862 | 0.3499 | 0.2999 | 0.3861 |
| $p_4$  | 0.4641 | 0.2499 | 0.0301 | 0.2360 |
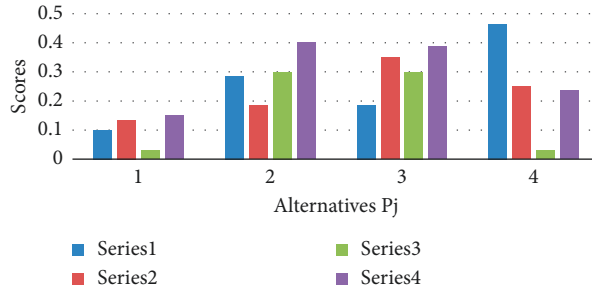


Figure 4: Score values of $\widetilde{x}_{cd}$ equivalent to the decision matrix $\widetilde{W}$.

Table 4: Reordering of the partial evaluations.

| Alternatives | Rearranging of the partial evaluations | Fuzzy measures |
|---|---|---|
| $p_2$ | $\widetilde{x}_{2(4)} \succ \widetilde{x}_{2(3)} \succ \widetilde{x}_{2(1)} \succ \widetilde{x}_{2(2)}$ | $''n(S_{2(1)}) = n(\{X_{(4)}\}) = 0.31, n(S_{2(2)}) = n(\{X_{(4)}, X_{(3)}\}) = 0.4279,$<br>$n(S_{2(3)}) = n(\{X_{(4)}, X_{(3)}, X_{(1)}\}) = 0.7354, n(S_{2(4)}) = n(\{X_{(4)}, X_{(3)}, X_{(1)}, X_{(2)}\}) = 1''$ |
| $p_3$ | $\widetilde{x}_{3(4)} \succ \widetilde{x}_{3(2)} \succ \widetilde{x}_{3(3)} \succ \widetilde{x}_{3(1)}$ | $''n(S_{3(1)}) = n(\{X_{(4)}\}) = 0.31, n(S_{3(2)}) = n(\{X_{(4)}, X_{(2)}\}) = 0.4828,$<br>$n(S_{3(3)}) = n(\{X_{(4)}, X_{(2)}, X_{(3)}\}) = 0.6755, n(S_{3(4)}) = n(\{X_{(4)}, X_{(2)}, X_{(3)}, X_{(1)}\}) = 1''$ |
| $p_4$ | $\widetilde{x}_{4(1)} \succ \widetilde{x}_{4(2)} \succ \widetilde{x}_{4(4)} \succ \widetilde{x}_{4(3)}$ | $''n(S_{4(1)}) = n(\{X_{(1)}\}) = 0.26, n(S_{4(2)}) = n(\{X_{(1)}, X_{(2)}\}) = 0.4845,$<br>$n(S_{4(3)}) = n(\{X_{(1)}, X_{(2)}, X_{(4)}\}) = 0.7834, n(S_{4(4)}) = n(\{X_{(1)}, X_{(2)}, X_{(4)}, X_{(3)}\}) = 1''$ |

Table 5: Associated weights of decision matrix $\widetilde{W}$.

|        | $X_1$  | $X_2$  | $X_3$  | $X_4$  |
|--------|--------|--------|--------|--------|
| $p_1$  | 0.2817 | 0.3521 | 0.1549 | 0.2113 |
| $p_2$  | 0.1788 | 0.4632 | 0.1508 | 0.2072 |
| $p_3$  | 0.1914 | 0.4037 | 0.1866 | 0.2183 |
| $p_4$  | 0.0817 | 0.3152 | 0.3259 | 0.2772 |

Table 6: Overall computation and ranking orders of INNs $\widetilde{x}_c$ for various $z$.

| $z$ | $\widetilde{x}_1$ | $\widetilde{x}_2$ | $\widetilde{x}_3$ | $\widetilde{x}_4$ | Ranking orders |
|---|---|---|---|---|---|
| 0.1 | $\langle[0.3609, 0.5192],$<br>$[0.2827, 0.3900],$<br>$[0.4899, 0.4909]\rangle$ | $\langle[0.5585, 0.6842],$<br>$[0.1929, 0.3513],$<br>$[0.3833, 0.4869]\rangle$ | $\langle[0.4613, 0.6704],$<br>$[0.2814, 0.3832],$<br>$[0.2110, 0.3844]\rangle$ | $\langle[0.5637, 0.7684],$<br>$[0.3139, 0.4989],$<br>$[0.1531, 0.3843]\rangle$ | $\widetilde{x}_2 \succ \widetilde{x}_3 \succ \widetilde{x}_4 \succ \widetilde{x}_1$ |
| 0.5 | $\langle[0.3688, 0.5160],$<br>$[0.2848, 0.3898],$<br>$[0.4879, 0.5791]\rangle$ | $\langle[0.5554, 0.6973],$<br>$[0.1996, 0.3652],$<br>$[0.3848, 0.5116]\rangle$ | $\langle[0.4503, 0.6697],$<br>$[0.2835, 0.3847],$<br>$[0.2222, 0.3880]\rangle$ | $\langle[0.5554, 0.7659],$<br>$[0.3105, 0.5013],$<br>$[0.1598, 0.3937]\rangle$ | $\widetilde{x}_2 \succ \widetilde{x}_3 \succ \widetilde{x}_4 \succ \widetilde{x}_1$ |
| 1.0 | $\langle[0.3693, 0.5109],$<br>$[0.2856, 0.3899],$<br>$[0.5001, 0.6091]\rangle$ | $\langle[0.5533, 0.6928],$<br>$[0.2019, 0.3727],$<br>$[0.3855, 0.5134]\rangle$ | $\langle[0.4594, 0.6645],$<br>$[0.2842, 0.3854],$<br>$[0.2256, 0.3916]\rangle$ | $\langle[0.5404, 0.7649],$<br>$[0.3334, 0.5029],$<br>$[0.1620, 0.3902]\rangle$ | $\widetilde{x}_2 \succ \widetilde{x}_3 \succ \widetilde{x}_4 \succ x_1$ |
| 1.5 | $\langle[0.3688, 0.5147],$<br>$[0.2859, 0.3896],$<br>$[0.4889, 0.5893]\rangle$ | $\langle[0.5510, 0.6806],$<br>$[0.2028, 0.3767],$<br>$[0.3859, 0.5145]\rangle$ | $\langle[0.4589, 0.6618],$<br>$[0.2847, 0.3858],$<br>$[0.2271, 0.3920]\rangle$ | $\langle[0.5477, 0.7645],$<br>$[0.3249, 0.5039],$<br>$[0.1620, 0.4002]\rangle$ | $\widetilde{x}_2 \succ \widetilde{x}_3 \succ \widetilde{x}_4 \succ \widetilde{x}_1$ |
| 2.0 | $\langle[0.3684, 0.5141],$<br>$[0.2861, 0.4009],$<br>$[0.5009, 0.6009]\rangle$ | $\langle[0.5512, 0.6892],$<br>$[0.2033, 0.3793],$<br>$[0.3861, 0.5152]\rangle$ | $\langle[0.4586, 0.6501],$<br>$[0.2849, 0.3850],$<br>$[0.2279, 0.3939]\rangle$ | $\langle[0.5450, 0.7641],$<br>$[0.3257, 0.5045],$<br>$[0.1636, 0.4060]\rangle$ | $\widetilde{x}_2 \succ \widetilde{x}_3 \succ \widetilde{x}_4 \succ \widetilde{x}_1$ |
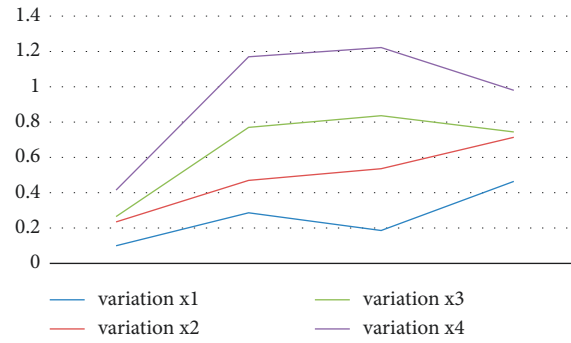
FIGURE 5: Total ranking of the four pixel sets with the help of the INHPCI operator based on Table 5.
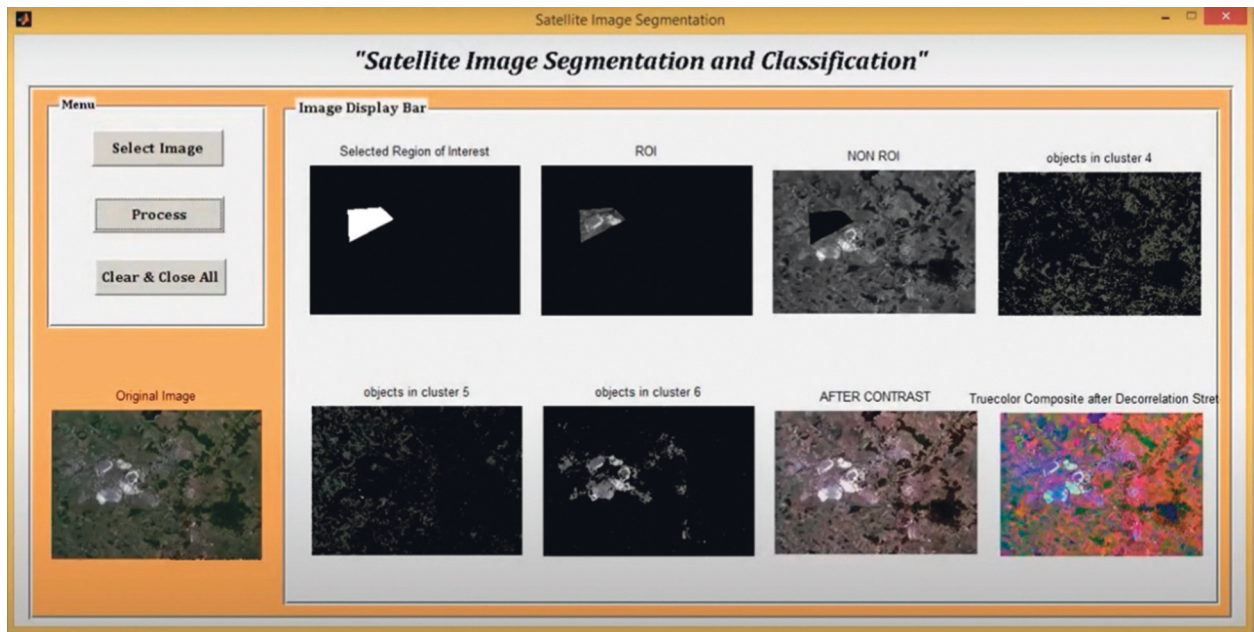


FIGURE 6: HGSCIO-FCM-based satellite image segmentation and classification application.

TABLE 7: The four features of four metals.

| Metal | $X_1$: color | $X_2$: hardness | $X_3$: property | $X_4$: appearance |
|---|---|---|---|---|
| Vanadium | Silvery-white | Ductile | Metallic-looking | Solid |
| Iron | Red-brown | Ductile | Metallic-looking | Solid |
| Copper | Red-brown | Nonductile | Metallic-looking | Solid |
| Nickel | Silvery-white | Ductile | Lustrous metal | Solid |

integral operators can be used for categorizing that smoke and haze primarily impact the visible bands, leaving the near-infrared (NIR) and short-wave infrared (SWIR) bands unaffected. Furthermore, the decision-making model proposed in this study may be incorporated to identify the deforestation area. This study will investigate the implementation aspects of these datasets to test accuracy of the postposed decision-making model in future.
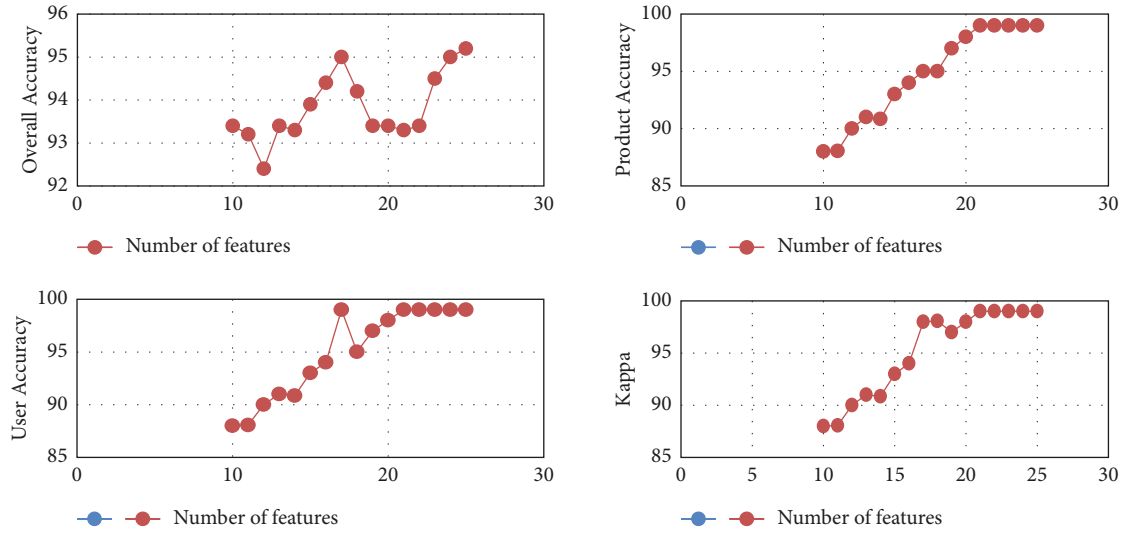
FIGURE 7: Classification accuracy of the four features using trained BPNN models that is using HGSCIO-FCM.
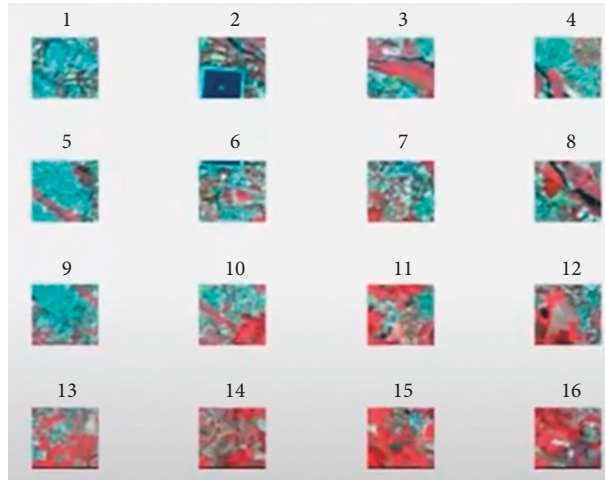


FIGURE 8: The classification process of an image in different stages of the implemented BPNN model that is using HGSCIO-FCM.
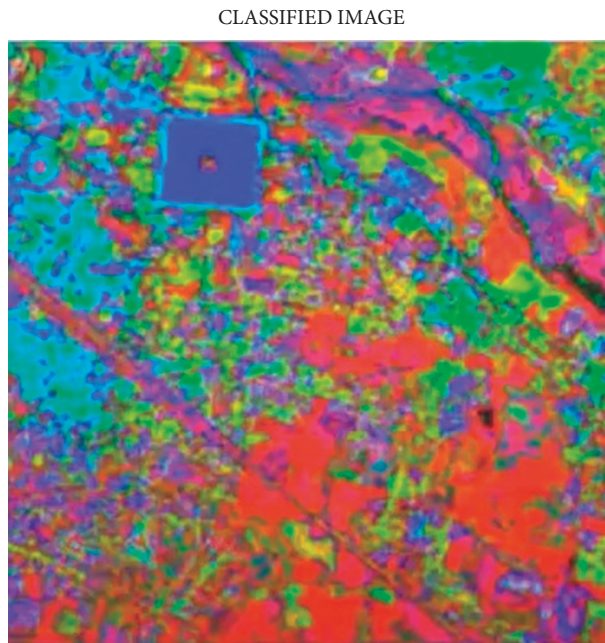
CLASSIFIED IMAGE



FIGURE 9: Final detection cluster of vanadium through the implemented model.

## 5. Conclusion

A novel BPNN model that is using the HGSCIO-FCM system for material classification to detect objects from satellite data is proposed in this study. The results provided from the experiments proved that the decision-making model using intuitionistic fuzzy Hamacher generalized Shapley Choquet integral operators for feature extraction and automatic material classification in mining area using satellite data shows encouraging performances in terms of material classification.

To the best of our knowledge, this is the first study making use of intuitionistic fuzzy Hamacher generalized Shapley Choquet integral operators for feature extraction and automatic material classification for satellite image classification problem.

Specifically, the main contributions of this study are as follows:

(i) The proposed approach is able to provide the satellite-based image clustering decisions making within narrow time intervals, which helps in addressing the geological decisions more systematically

(ii) We propose a new fuzzy Hamacher generalized Shapley Choquet integral operators-based BPNN architecture for the feature extraction process, in which the model structure is not too deep and the results

(iii) Furthermore, deep feature classification using artificial neural networks (ANNs) models such as back propagation neural networks has been employed to improve the classification performance

(iv) Regarding the experiment, a USGS Landsat 8 Level 2, Collection 2, Tier 1 (LANDSAT/LC08/C02/T1) dataset has been considered to evaluate the proposed approach. The collected data contain standardized reference grid of overlapping images with 170 km × 183 km.

(v) Specifically, we defined a novel automated material classification method by employing the decision-making capabilities of fuzzy Hamacher generalized Shapley Choquet integral operators

## Data Availability

The data used to support the findings of this study are available from the corresponding authors upon request.

## Disclosure

This study was performed for the academic purpose of Ho Technical University, Ho, Ghana.

## Conflicts of Interest

The authors declare that there are no conflicts of interest.

## References

[1] B. Boulassel, N. Sadeg, O. Roussel, M. Perrin, and H. B. Tahar, "Fatal poisoning by vanadium," *Forensic Science International*, vol. 206, pp. 79–81, 2011.

[2] A. W. Musk and J. G. Tees, "Asthma caused by occupational exposure to vanadium compounds," *Medical Journal of Australia*, vol. 1, no. 4, pp. 183-184, 1982.

[3] C. Zenz and B. A. Berg, "Human responses to controlled vanadium pentoxide exposure," *Archives of Environmental Health: An International Journal*, vol. 14, no. 5, pp. 709–712, 1967.

[4] A. J. Ghio, R. Silbajoris, J. L. Carson, and J. M. Samet, "Biologic effects of oil fly ash," *Environmental Health Perspectives*, vol. 110, no. 1, pp. 89–94, 2002.

[5] R. Hauser, S. Elreedy, P. B. Ryan, and D. C. Christiani, "Urine vanadium concentrations in workers overhauling an oil-fired boiler," *American Journal of Industrial Medicine*, vol. 33, no. 1, pp. 55–60, 1998.

[6] J. Cortijo, V. Villagrasa, M. Martí-Cabrera et al., "The spasmogenic effects of vanadate in human isolated bronchus," *British Journal of Pharmacology*, vol. 121, no. 7, pp. 1339–1349, 1997.

[7] M. Z. Mehdi, S. K. Pandey, J. F. Thberge, and A. K. Srivastava, "Insulin signal mimicry as a mechanism for the insulin-like effects of vanadium," *Cell Biochemistry and Biophysics*, vol. 44, pp. 73–81, 2006.

[8] S. M. Brichard and J. C. Henquin, "The role of vanadium in the management of diabetes," *Trends in Pharmacological Sciences*, vol. 16, pp. 265–270, 1995.

[9] P. C. Pandey and B. Bhattacharya, "Future Perspectives and Challenges in Hyperspectral Remote Sensing," *Hyperspectral Remote Sensing*, vol. 21, 2020.

[10] Z. Zhang, P. Tang, and T. Corpetti, "Satellite image time series clustering via affinity propagation," in *Proceedings of the 2016 IEEE International Geoscience and Remote Sensing Symposium (IGARSS)*, pp. 2419–2422, IEEE, Beijing, China, 10 July 2016.

[11] A. Pugazhenthi and L. S. Kumar, "Cloud extraction from INSAT-3D satellite image by K-means and fuzzy C-means clustering algorithms," in *Proceedings of the 2020 International Conference on System, Computation, Automation and Networking (ICSCAN)*, pp. 1–4, IEEE, Pondicherry, India, July 2020.

[12] P. K. Guru Diderot, N. Vasudevan, and K. S. Sankaran, "An efficient fuzzy C-means clustering based image dissection algorithm for satellite images," in *Proceedings of the 2019 International Conference on Communication and Signal Processing (ICCSP)*, pp. 0806–0809, IEEE, Chennai, India, 4 April 2019.

[13] J. Alvarez and B. Walls, "Constellations, clusters, and communication technology: expanding small satellite access to space," in *Proceedings of the 2016 IEEE Aerospace Conference*, pp. 1–11, IEEE, Big Sky, MT, USA, 5 March 2016.

[14] G. Kumar, P. P. Sarthi, P. Ranjan, and R. Rajesh, "Performance of k-means based satellite image clustering in RGB and HSV color space," in *Proceedings of the 2016 International Conference on Recent Trends in Information Technology (ICRTIT)*, pp. 1–5, IEEE, Chennai, India, 8 April 2016.

[15] T. Yairi, N. Takeishi, T. Oda, Y. Nakajima, N. Nishimura, and N. Takata, "A data-driven health monitoring method for satellite housekeeping data based on probabilistic clustering and dimensionality reduction," *IEEE Transactions on*

*Aerospace and Electronic Systems*, vol. 53, no. 3, pp. 1384–1401, June 2017.

[16] David Shultz et al., "Colony: a new business model for research and development," in *Proceedings of the 24th Annual AIAA/USU Conference on Small Satellites*, August 2010.

[17] "The Future of High Throughput Satellites for Service Providers," November 27 2013, http://www.newtec.eu/article/article/the-future-of-high-throughput-satellites-for-service-providers.

[18] Wu Xian-De, D. Hong, and S. Zhao-Wei, "The database design in ground test system of micro-satellite cluster," in *Proceedings of the 2009 4th IEEE Conference on Industrial Electronics and Applications*, pp. 4008–4012, IEEE, Xi'an, China, 25 May 2009.

[19] R. Radhakrishnan, W. W. Edmonson, F. Afghah, R. M. Rodriguez-Osorio, F. Pinto, and S. C. Burleigh, "Survey of inter-satellite communication for small satellite systems: physical layer to network layer view," *IEEE Communications Surveys & Tutorials Fourthquarter*, vol. 18, no. 4, pp. 2442–2473, 2016.

[20] H. Wang, F. Smarandache, Y. Zhang, and R. Sunderraman, "Single Valued Neutrosophic Sets," *Technical Sciences and Applied Mathematics*, 2012.

[21] R. H. Ahmed and Y. Guo, "Neutrosophic Set in Medical Image Clustering," *Neutrosophic Set in Medical Image Analysis*, 2019.

[22] B. Banerjee and K. M. Buddhiraju, "Satellite image segmentation: a novel adaptive mean-shift clustering based approach," in *Proceedings of the 2012 IEEE International Geoscience and Remote Sensing Symposium*, pp. 4319–4322, IEEE, Munich, Germany, 22 July 2012.

[23] H. Wang, F. Smarandache, R. Sunderraman, and Y. Q. Zhang, "Interval neutrosophic sets and logic: theory and applications in computing: theory and applications in computing," *Infinite Study*, vol. 5, 2005.

[24] R. Sahin, "Multi-criteria neutrosophic decision making method based on score and accuracy functions under neutrosophic environment," 2014, https://arxiv.org/abs/1412.5202.

[25] Z. Xu, "On method for uncertain multiple attribute decision making problems with uncertain multiplicative preference information on alternatives," *Fuzzy Optimization and Decision Making*, vol. 4, no. 2, pp. 131–139, 2005.

[26] H. Hamacher, "Uber logische verknupfungen unscharfer aussagen und deren zugehörige bewertungsfunktionen," *Progress in Cybernetics and Systems Research*, vol. 3, pp. 276–288, 1978.

[27] M. Sugeno, "Theory of Fuzzy Integrals and its Applications," PhD. Thesis, Tokyo Institute of Technology, Tokyo, 1974.

[28] T. Murofushi and M. Sugeno, "An interpretation of fuzzy measures and the Choquet integral as an integral with respect to a fuzzy measure," *Fuzzy Sets and Systems*, vol. 29, no. 2, pp. 201–227, 1989.

[29] H. X. Sun, H. X. Yang, J. Z. Wu, and Y. Ouyang, "Interval neutrosophic numbers Choquet integral operator for multi-criteria decision making," *Journal of Intelligent and Fuzzy Systems*, vol. 28, no. 6, pp. 2443–2455, 2015.

[30] P. Kakati and S. Rahman, "Decision making model for medical diagnosis based on some new interval neutrosophic hamacher power Choquet integral operators,".

[31] J. Dombi, "A general class of fuzzy operators, the DeMorgan class of fuzzy operators, and fuzziness measures induced by fuzzy operators," *Fuzzy Sets and Systems*, vol. 8, no. 2, pp. 149–163, 1982.

[32] M. Gunasekaran and S. Ganeshmoorthy, "OCR recognition system using feed forward and back propagation neural network," in *Proceedings of the Second National Conference on Signal Processing Communications and VLSI Design - NCSCV'10*, pp. 345–350, Conal, Coimbatore, India, 7 May 2010.

[33] "USGS Landsat Satellite Missions," Landsat Satellite Missions, 2022, https://www.usgs.gov/landsat-missions/landsat-satellite-missions/accessed.

[34] "USGS EarthExplorer," EarthExplorer, 2022, https://earthexplorer.usgs.gov/accessed.

[35] "NASA Landsat Science," The Thematic Mapper, 2013, https://landsat.gsfc.nasa.gov/article/the-thematic-mapper/accessed.